RSC Advances

PAPER

View Article Online
View Journal | View Issue

Cite this: *RSC Adv.*, 2025, **15**, 13442

A Spin-polarized DFT study of functionalized MXenes as effective anchor materials in lithium-sulfur batteries†

Yize Niu, Ying Jiang, Feihu Zou, Weiqi Song, Yue Zhao, Hongye Zhang, Qiang Li * and Yuanyuan Pan *

Lithium-sulfur (Li-S) batteries have attracted great enthusiasm in recent years due to ultra-high theoretical energy densities, abundant sulfur electrode resources and low price. Despite the severe shuttle effect of lithium polysulfides (LiPSs), the poor conductivity of S_8 and its intermediate products, and the relatively slow dynamics, pose significant challenges for the commercial application of Li-S batteries. Here, functionalized MXenes M_2CT_2 (M = V, Cr, Mn, and Mo; T = F and O) used as the sulfur host are studied to build multifunctional cathodes *via* spin-polarized first-principles calculation. Through analyzing the adsorption energy and configuration of S_8/Li_2S_n adsorbed M_2CT_2, it is found that spin polarization is indispensable to the Li-S battery calculation of MXenes with transition metals. With the spin polarization calculation, the M_2CT_2 exhibit moderate anchoring strengths and stable adsorption structures, which effectively mitigates the polysulfide shuttle phenomenon. The low decomposition barriers of Li_2S (0.27–1.00 eV) and low diffusion barriers of Li^+ (0.11–0.44 eV) of M_2CT_2 are observed, which effectively improve the rate performance of batteries. Among the studied MXenes, V_2CO_2 and Mo_2CO_2 are the best choices of host materials for LiPSs with metallic characteristics, outstanding electrocatalysis performance, low decomposition barriers of Li_2S, and diffusion barriers of Li^+. This work provides important insights into spin-polarized electrode materials for enhanced energy storage capabilities by investigating the application of intrinsic magnetic MXene compounds.

Received 26th February 2025
Accepted 20th April 2025

DOI: 10.1039/d5ra01387a

rsc.li/rsc-advances

Introduction

With the continuous growth of energy demand, it is an urgent task to develop high-performance and affordable rechargeable batteries. Lithium-sulfur (Li-S) batteries have attracted substantial research interest in recent years, owing to their high theoretical capacity and specific energy.[1–4] Based on the two-electron transfer redox reaction involving multiple steps, the theoretical capacity of Li-S batteries can reach up to 1675 mA h g^{-1}. Moreover, sulfur is abundant on earth and inexpensive.[5,6] As a result, the combination of high theoretical capacity and low cost endows Li-S batteries with great application potential in the field of commercial batteries.[7] However, there is still a long journey ahead for Li-S batteries to achieve commercial application, which is hindered by several thorny issues. For example, the electrical conductivities of S_8 and Li_2S_n are poor, and the reaction kinetics is sluggish due to the high decomposition energy barrier of Li_2S.[8,9] During the cycling process, intermediate products of lithium polysulfides (LiPSs) are constantly generated. These intermediates can dissolve in the electrolyte, resulting in a reduction of active sulfur species. In particular, long-chain LiPSs (Li_2S_n, n = 4, 6, and 8) will migrate to the lithium metal anode and deposit there by shuttling through the separator, which also results in a rapid decline in the battery's capacity.[10,11] In the future, more efforts should be devoted to suppressing the shuttle effect. An ideal sulfur composite cathode is capable of suppressing the shuttle effect by moderately anchoring Li_2S_n, enhancing the sulfur reduction reaction (SRR), and improving the reaction kinetics.[12–14]

MXenes, a novel class of two-dimensional transition metal carbides and nitrides, exhibit remarkable capabilities in electrochemical energy storage systems. These materials combine metallic-grade conductivity with ultrafast charge migration kinetics and exceptional surface charge storage capacity, attributes that have positioned them at the forefront of energy research since their 2011 discovery.[15] Following Gogotsi's pioneering synthesis of Ti_3C_2 in 2011, titanium-based MXenes have dominated Li-S battery research due to their exceptional interfacial compatibility and sulfur confinement capabilities.[16] After the first synthesis of Ti_3C_2, M_3C_2 has been extensively studied and is considered to be a cathode material for Li-S batteries with excellent performance. Recent experimental studies proved that M_2C is thinner than M_3C_2, which has also proven to be a good

College of Physics, Center for Marine Observation and Communications, Qingdao University, Qingdao, China. E-mail: liqiang@qdu.edu.cn; panyy@qdu.edu.cn

† Electronic supplementary information (ESI) available. See DOI: https://doi.org/10.1039/d5ra01387a

anchoring material for Li-S batteries with high specific capacity and long cycle life.[17,18] MXenes synthesized *via* HF etching typically exhibit surface terminations dominated by oxygen (O) and fluorine (F) groups, which could enhance material stability, optimize interface interaction and improve electrochemical performance.[19,20] According to previous reports, $Ti_2C(OH)_2$ and $V_2C(OH)_2$ exhibit excessively strong interfacial interactions with LiPSs, inducing premature decomposition of active species.[21,22] Conversely, oxygen-terminated MXenes like Ti_2CO_2 and Ti_2NO_2 demonstrate optimal chemisorption energetics for LiPSs anchoring. Ti_2CF_2 and Ti_2NF_2 achieve balanced binding interactions, with systematic analyses revealing that O- and F-terminated MXenes collectively offer superior polysulfide confinement capabilities compared to OH-terminated MXenes.[23,24] The interaction between the polysulfides and the hydroxide-ternibated or no functionalized MXene is very strong, which could distort the polysulfides and the MXene materials. Therefore, they cannot effectively suppress the shuttle effect.[25–27] Recently, V_2NO_2 and V_2NF_2 MXenes have been widely investigated due to low decomposition barriers of Li_2S and diffusion barriers of Li^+, which could accelerate reaction kinetics during the discharge and charging process. The structural diversity of MXenes motivates systematic exploration of their electrochemical properties, particularly focusing on surface-engineered variants with functional groups. It is an interesting task to explore other MXene materials that possess outstanding electrochemical performance, particularly those MXene materials with a large number of functional groups and those that have undergone surface modification.[28,29]

In our work, a series of M_2CT_2 (M = V, Cr, Mn, and Mo; T = F and O) are selected as sulfur hosts to construct multifunctional cathode material *via* spin-polarized first-principles calculations. We note the adsorption energy of S_8/Li_2S_n adsorbed M_2CT_2 is greatly reduced from non-spin-polarized system to spin-polarized system. Spin-polarized systems provide a critical framework for comprehensively elucidating interfacial phenomena in transition metal composites at atomic scales. The adsorption energy of S_8/Li_2S_n adsorbed M_2CT_2 range from 0.63 eV to 5.15 eV, which indicates the M_2CT_2 could inhibit the shuttle effect and reduce the loss of active sulfur species in the polarization system. We find that S_8 can be efficiently reduced to Li_2S with a small rare-limiting step (0.51–1.37 eV), indicating the superior sulfur reducing ability of M_2CT_2. Moreover, the decomposition barriers of Li_2S and migration barriers of Li^+ for M_2CO_2 are lower than those for M_2CF_2 during charging process, which ultimately promotes redox kinetics during cycling. Based on the finding presented above, we identified V_2CO_2 and Mo_2CO_2 as promising candidates for host materials with moderate anchoring strength and excellent electrocatalytic performance. Systematic analysis of MXene functionalities in this work provides actionable strategies for tailoring their interfacial properties toward sulfur cathode optimization.

Computational details

Spin-polarized density functional theory (DFT) calculations are carried out using the Vienna *Ab Initio* Simulation Package (VASP), employing the Perdew–Burke–Ernzerhof (PBE) generalized gradient approximation (GGA) functional to describe exchange-correlation effects.[30,31] The core-electron interactions are treated through the projector-augmented wave (PAW) methodology, with a plane-wave basis set truncated at 500 eV kinetic energy. For Brillouin zone integration in the 4×4 supercell's two-dimensional geometry, a Monkhorst–Pack grid of $5 \times 5 \times 1$ *k*-points is implemented.[32] To better characterize the strongly correlated 3d electron systems, we incorporate the Hubbard U correction within the GGA + U framework.[33] According to the previous works, the U values of V, Cr, Mn, and Mo atoms are set to be 3, 4, 3, and 3 eV, respectively.[22,34–36] Long-range van der Waals interactions are accounted for using the DFT-D3 empirical dispersion correction scheme.[37] A minimum vacuum spacing of 20 Å perpendicular to the surface plane is maintained to eliminate artificial periodic interactions. Structural optimizations are performed until achieving convergence thresholds of 1.0×10^{-5} eV per atom for total energy and 0.01 eV $Å^{-1}$ for residual forces. The migration mechanisms of Li^+ on M_2CT_2 surfaces are investigated through the climbing image nudged elastic band (CI-NEB) method, which enables precise determination of minimum energy pathways and activation barriers.[38] The thermodynamic stability of Li_2S adsorption on V_2CO_2 and Mo_2CO_2 is simulated by *ab initio* molecular dynamics (AIMD) at 300 K. The NVT ensemble simulations are conducted for 5 ps with a time step of 1.0 fs, corresponding to 5000 simulation steps. Detailed calculation equation of adsorption energies (E_{ads}), charge density difference (CDD), and the equations of Gibbs free energy change (ΔG) are comprehensively derived in the ESI† section.

Results and discussions

Configuration, magnetic ground state and electronic conductivity of M_2CT_2

Investigating MXenes with different magnetic transition metal constituents offers a strategic pathway to leverage their compositional versatility for improving sulfur electrochemistry in Li-S systems. Therefore, the $M_2C(F/O)_2$ with the transition metals (M = V, Cr, Mn, and Mo) are chosen as sulfur hosts in our work. The monolayer M_2C MXene adopts a *P*3*m*1-symmetric honeycomb lattice, featuring a stratified architecture where hexagonally arranged carbon atoms are intercalated between two metallic M layers, as structurally resolved in Fig. 1a.[39] There are five possible configurations for terminal groups (T = F and O) absorbed on the M atom in Fig. S1†: (a) T atoms locate right above the M atoms (Top sites); (b) T atoms locate at the hollow sites of adjacent C atoms (Hcp sites); (c) T atoms locate at the hollow sites of contralateral M atoms (Fcc sites); (d) T atoms located at the Fcc and Hcp sites (Fcc–Hcp); (e) T atoms located at the Hcp and Top sites (Fcc–Hcp). The stable configurations of M_2CT_2 are Fcc structures, except for Cr_2CO_2 and Mo_2CO_2, which are Hcp structures as shown in Fig. 1c. The basic information of their lattice parameters is listed in Table S1.†

Considering that magnetic transition metal in the M_2CT_2, five types of magnetic ground state structures are calculated in Fig. 2: non-magnetic (NM), ferromagnetic (FM), and

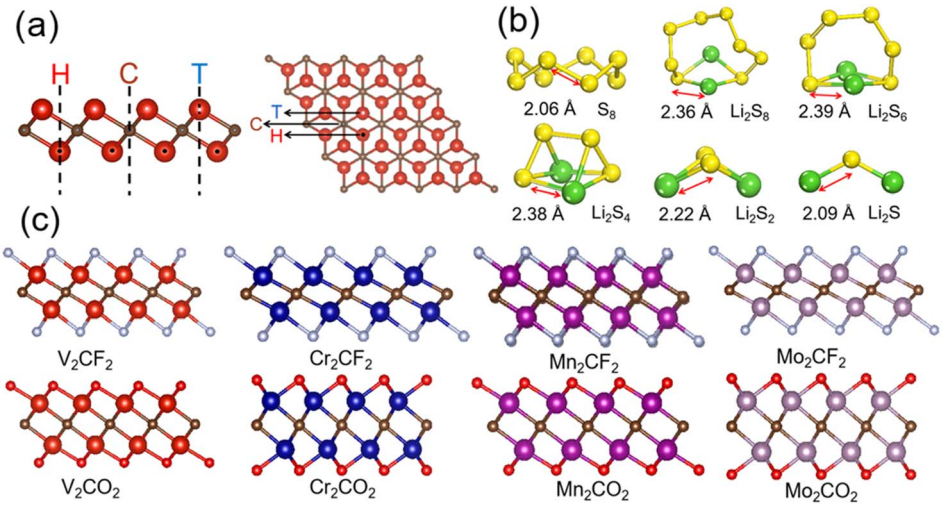

Fig. 1 (a) Top and side views of MXene monolayer with different adsorption sites (hollow site (H), carbon-top site (C) and transition metal-top (T)). (b) Geometrical structures of S_8 and Li_2S_n molecules. (c) Side view of the stable atomic structures of V_2CT_2, Cr_2CT_2, Mn_2CT_2, and Mo_2CT_2 with the terminal groups T = O and F. Yellow, green, dark red, brown, light red, white, blue, dark purple and light purple color balls represent the S, Li, V, C, O, F, Cr, Mn and Mo atoms, respectively.

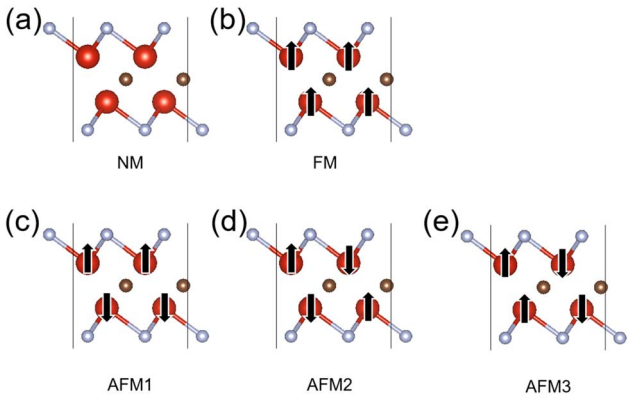

Fig. 2 Magnetic state configurations of M_2CT_2: (a–e) NM, FM, AFM1, AFM2, AFM3, respectively (taking a 2 × 2 V_2CF_2 supercells as an example). The directions of the arrow represent the spin up and down.

antiferromagnetic (AFM1, 2, and 3). After relaxation, it is found that stable structures of V_2CO_2 and Mo_2CO_2 are NM, while the stable structures of other M_2CT_2 are AFM, except that Mn_2CF_2 and Cr_2CO_2 are FM structures. The calculated magnetic ground states are same as the results of the previous studies.[34,40–42] According to the crystal field theory, the magnetic exchange interactions in the 2D magnetic materials mainly originate from two kinds of mechanisms:[43–45] (i) the super-exchange ferromagnetism between the nearest intra-layered M atoms *via* the outmost oxygen atom (*e.g.*, Cr–O–Cr and Mn–F–Mn). (ii) The antiferromagnetic interactions between the nearest interlayered M atoms *via* the carbon atom (*e.g.* Cr–C–Cr and Mn–C–Mn). In this case, the ferromagnetic super-exchange processes start to compete with the antiferromagnetic super-exchange mechanism.

Meanwhile, the limited conductivity of sulfur represents another key challenge impeding the advancement of Li-S batteries. To further study the electronic structural properties of M_2CT_2, we calculate the projected density of states (PDOS) of M_2CT_2. As shown in Fig. 3, V_2CO_2 and Mo_2CO_2 show significant metallic conductivity, while the others are semiconductors, except for Mn_2CF_2, which is a special semimetal. The DOS of the M_2CT_2 mainly comes from the d-orbital of the transition metal. Furthermore, it is found that the d_{xy} and $d_{x^2-y^2}$ orbitals are degenerated, while the d_{xz} and d_{yz} orbitals are degenerated at their respective energy levels as presented in Fig. S2.†

Anchoring of M_2CT_2 to inhibit shuttle effect

During Li-S battery discharge, LiPSs dissolve into the electrolyte and shuttle toward the anode through the separator, leading to progressive depletion of electroactive sulfur species. Optimal cathode materials require appropriate adsorption energies to immobilize LiPSs and prevent active sulfur depletion.[46,47] Before to study the anchor ability of M_2CT_2 for S_8 and Li_2S_n, the S_8 and Li_2S_n are optimized in 10 × 10 × 10 Å^3 cell, and the relaxed structures are shown in Fig. 1b. The S–S bond length in S_8 is determined to be 2.06 Å. The Li–S bond lengths in Li_2S_8, Li_2S_6, Li_2S_4, Li_2S_2 and Li_2S are determined to be 2.36 Å, 2.39 Å, 2.38 Å, 2.22 Å and 2.09 Å, respectively. These structures of our work are consistent with the previous reports.[40,48,49]

To evaluate the anchor performance of the functionalized M_2CT_2, we calculated the adsorption energy (E_{ads}) of S_8 and Li_2S_n on these M_2CT_2 surface as a key parameter, which is defined in the ESI.† The positive values of the adsorption energies indicate that adsorption could proceed spontaneously, and moderate adsorption energy represents good anchoring ability. The E_{ads} with spin-polarized and non-spin-polarized calculations are listed in Table 1 and Table S2,† respectively. The calculated E_{ads} for S_8 and Li_2S_n on V_2CT_2 and Cr_2CT_2 are well consistent with those from the previous report.[50] For the adsorption of the S_8 and Li_2S_n, a similar binding trend is

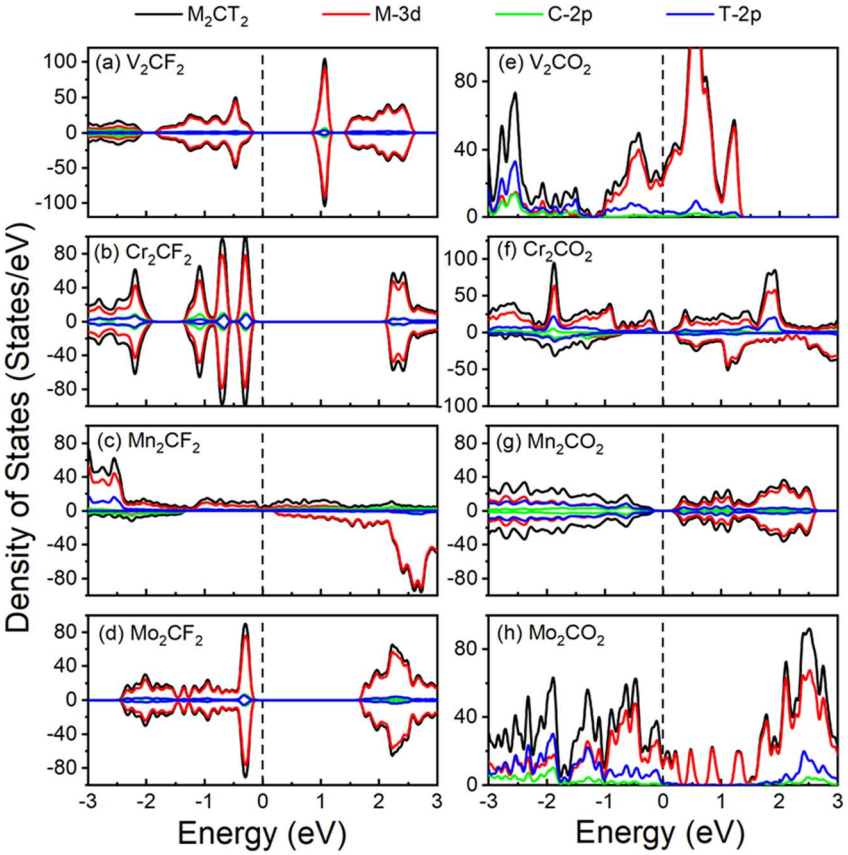

Fig. 3 Projected density of states of (a) V_2CF_2, (b) Cr_2CF_2, (c) Mn_2CF_2, (d) Mo_2CF_2, (e) V_2CO_2, (f) Cr_2CO_2, (g) Mn_2CO_2, and (h) Mo_2CO_2. The Fermi level is set at zero.

Table 1 The absorption energies E_{ads} (eV) of the S_8 and LiPSs on M_2CF_2 and M_2CO_2 with the spin-polarized calculations

MXene	S_8	Li_2S_8	Li_2S_6	Li_2S_4	Li_2S_2	Li_2S
V_2CF_2	0.80	1.14	1.05	1.47	2.08	2.27
Cr_2CF_2	0.76	1.01	0.97	0.91	1.24	1.41
Mn_2CF_2	0.63	1.17	1.16	1.99	2.35	2.58
Mo_2CF_2	0.88	1.19	1.12	1.10	1.72	2.50
V_2CO_2	1.02	2.07	2.02	3.30	3.48	4.37
Cr_2CO_2	1.04	2.40	2.12	3.64	4.10	3.73
Mn_2CO_2	0.89	2.37	2.30	3.70	4.27	4.01
Mo_2CO_2	1.38	3.44	3.13	4.38	4.24	5.15

observed in all the calculated M_2CT_2 as shown in Fig. 4. For all the calculated M_2CT_2, the E_{ads} values of the S_8 are comparable. In addition, we note that the E_{ads} values increase with a decrease in the size of LiPSs.

It is also found that the E_{ads} of S_8 and Li_2S_n on M_2CT_2 surface with the spin-polarized calculations are significantly reduced compared with those of the non-spin-polarized calculations. The E_{ads} of Li_2S_n on V_2CF_2 and Mn_2CF_2 are reduced by 0.73–1.14 eV from the non-spin-polarized system to the spin-polarized system, while the E_{ads} values of Li_2S_n absorbed on Cr_2CO_2 decreases by 0.62–2.44 eV. Meanwhile, the E_{ads} of Li_2S_n absorbed on Cr_2CF_2 and Mo_2CF_2 decreases by 2.10–3.55 eV, which is nearly three times that of V_2CF_2 and Mn_2CF_2.[50–52] The effect of the spin-polarization also reflected from the relaxed configuration of M_2CT_2–S_8/Li_2S_n. As presented in Fig. 5 and Fig. S3.† The atomic structure of Mn_2CO_2 cannot even maintain at the NM state. The short-chain polysulfides break their bonds, and the substrate M_2CT_2 undergo severe deformation under the spin-polarized calculation. The spin polarization system has a significant effect on the absorption process for the magnetic M_2CT_2. Therefore, we take the accurate spin-polarized calculation in the subsequent. The adsorption strength of the M_2CT_2 for Li_2S_n follows the sequence: Mn_2CF_2 > V_2CF_2> Mo_2CF_2 > Cr_2CF_2 and Mo_2CO_2 > Mn_2CO_2 > Cr_2CO_2 > V_2CO_2, respectively. It clearly shows that the E_{ads} of S_8/Li_2S_n on M_2CT_2 are much smaller than that on M_2C.[52] The enhanced covalent bonding characteristics between Li and S atoms in low-order LiPSs facilitate accelerated electron transfer from Li to S, creating vacant d-orbitals capable of accepting electrons from transition metal (T) atoms. Computational analyses reveal that short-chain LiPSs (Li_2S_2/Li_2S) and Li_2S_4 adopt specific geometric arrangements where dual lithium atoms remain proximal to the substrate surface, demonstrating strong chemisorption behavior. Conversely, long-chain species (Li_2S_8 and Li_2S_6) exhibit monodentate adsorption configurations with a single lithium atom near the interface, accompanied by horizontally oriented S_8 molecular adsorption. Crucially, all adsorbed LiPSs

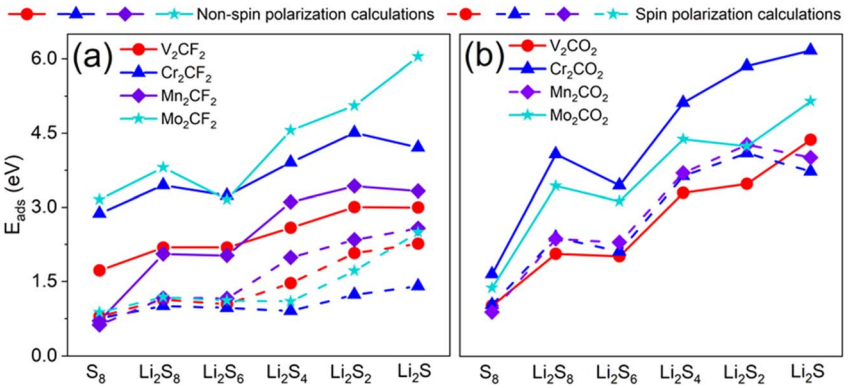

Fig. 4 The absorption energies of S_8/Li_2S_n absorbed on (a) M_2CF_2 and (b) M_2CO_2 monolayer. The dotted and solid lines represent the absorption energy with the spin-polarized and the non-spin-polarized calculations, respectively.

configurations maintain structural integrity during electrochemical cycling, showing no signs of dissociation. It ensures reliable polysulfide retention on M_2CT_2 surfaces throughout charge/discharge processes.

To effectively suppress polysulfide shuttling, the adsorption energetics of high-order Li_2S_n ($n = 4$, 6, and 8) on the sulfur host matrix should surpass those with conventional ether-based electrolytes 1,3-dioxolane/1,2-dimethoxyethane (DOL/DME), thereby preventing electrolyte-mediated active material dissolution and capacity fade.[53] Given the preferential solubility of high-sulfur-content LiPSs in organic electrolytes, we systematically evaluated the adsorption energetics of long-chain LiPSs

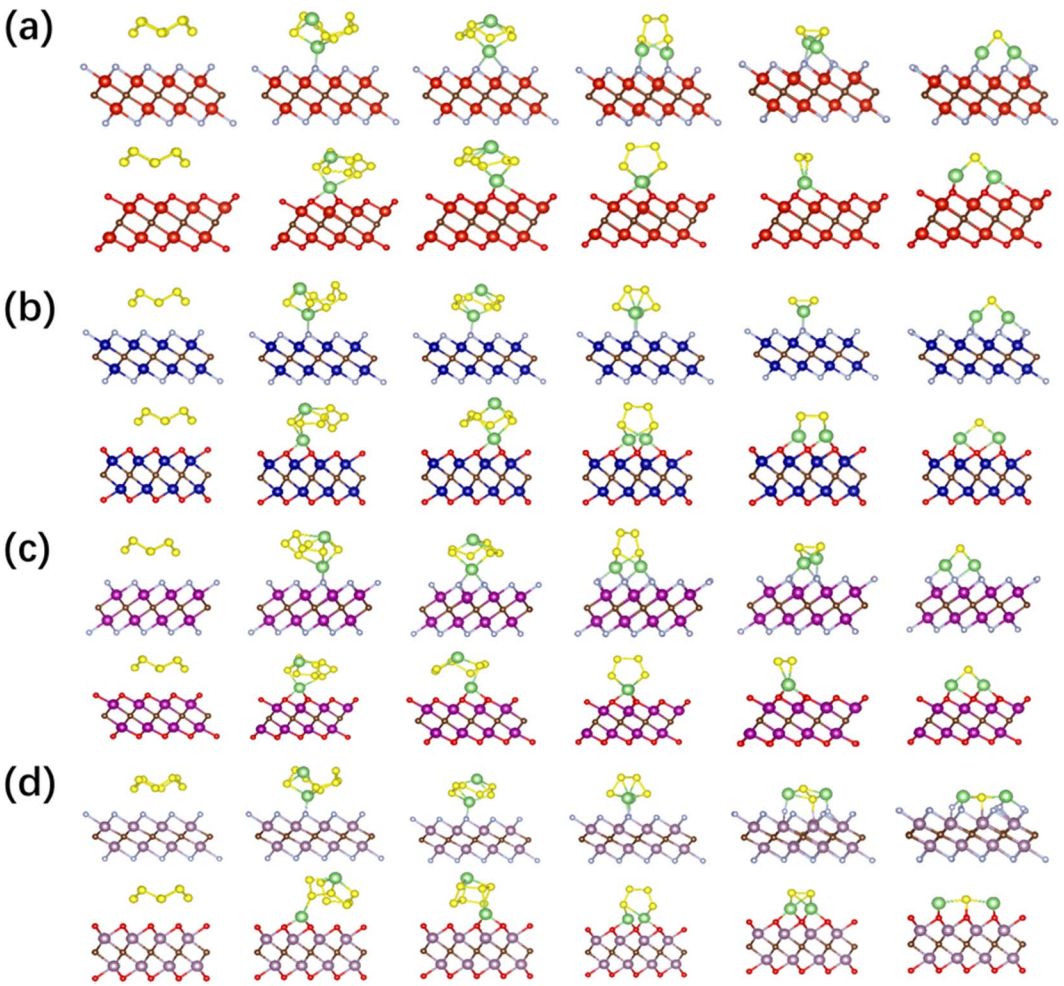

Fig. 5 The optimized structures of S_8/Li_2S_n adsorption on (a) V_2CT_2, (b) Cr_2CT_2, (c) Mn_2CT_2, and (d) Mo_2CT_2 monolayer with the spin-polarized calculations.

(Li_2S_8, Li_2S_6, and Li_2S_4) on DOL and DME. Structural optimizations of both isolated electrolyte molecules and LiPS-anchored complexes are shown in Fig. S4,† which reveal comparable polysulfide-trapping capabilities between DOL and DME, with adsorption energies spanning 0.75–0.90 eV. These values are significantly lower than those observed for M_2CO_2 substrates and marginally reduced compared to M_2CF_2 interfaces, highlighting the limited chemical confinement capacity of organic electrolytes relative to engineered MXene surfaces. Based on the aforementioned analysis, M_2CT_2 is capable of anchoring S_8/Li_2S_n with a suitable E_{ads} value, while, it can preserve the integrity of the adsorption structures. In a tug-of-war with solvent molecules, M_2CO_2 shows stronger chemical affinity for the LiPSs, which reveals its potential to serve as a type of host material for sulfur cathodes.

In order to explore the essence of the adsorption behavior between S_8/Li_2S_n and the surface of M_2CT_2, the CDD between M_2CT_2 monolayer and S_8/Li_2S_n are calculated as shown in Fig. 6 with the calculation details located in ESI†. The S_8 and M_2CF_2 interface exhibits negligible charge transfer, signifying the absence of chemical bond formation between the adsorbed sulfur species and the substrate. In contrast, S_8/Li_2S_n adsorption on M_2CO_2 exhibits significantly enhanced interfacial electron redistribution. Lithiation induces pronounced electron accumulation at Li_2S_n/M_2CT_2 interfaces, accompanied by intensified charge transfer indicative of Li–T (T = F/O) covalent bond formation. Concurrently, expanding electron-deficient domains within Li_2S_n reflect destabilization of Li–S and S–S bonding interactions. It can be deduced that chemical bonds are established between Li_2S_n and M_2CT_2 during the lithiation process, which agrees with the trend of the adsorption energy. Moreover, the decomposition pathways of LiPSs are critically governed by two concurrent mechanisms: interfacial stabilization through Li–T (T = F/O) covalent bond formation and structural destabilization *via* progressive cleavage of Li–S and S–S bonds within Li_2S_n species.

The electronic structures of the substrate undergo changes following LiPSs adsorption, which is investigated by analyzing

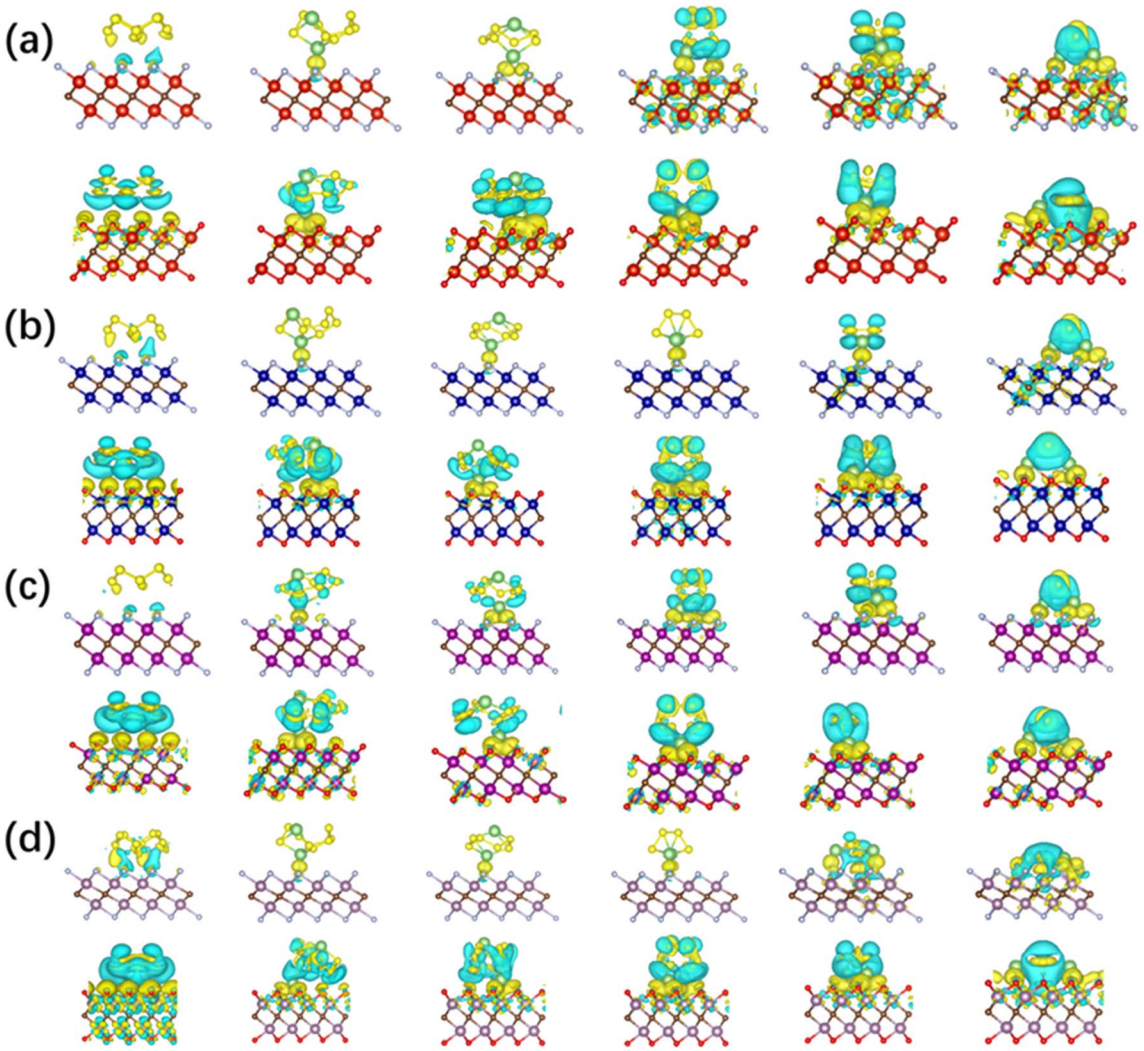

Fig. 6 Side views of CDD maps of S_8 and Li_2S_n on (a) V_2CT_2, (b) Cr_2CT_2, (c) Mn_2CT_2, and (d) Mo_2CT_2 monolayer (isosurface = ± 0.002 au for Li_2S_n, and isosurface = ± 0.0002 au for S_8). The yellow and blue region indicate electron accumulation and depletion, respectively.

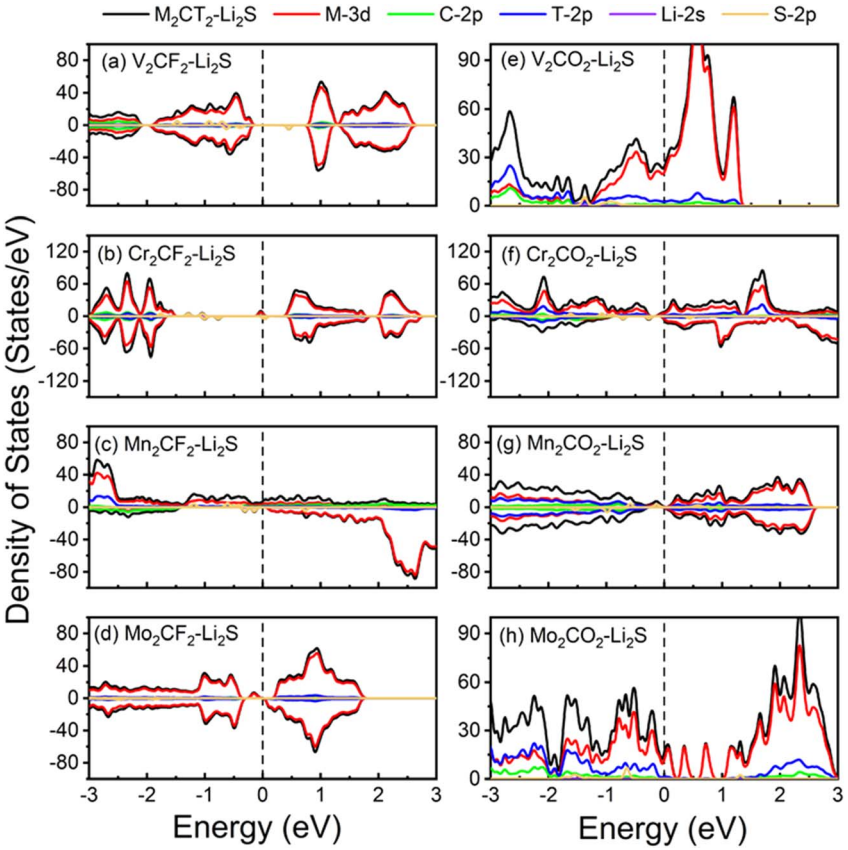

Fig. 7 Projected density of states of (a–h) M_2CT_2 monolayer after the adsorption of Li_2S, respectively. The Fermi level is set at zero.

the PDOS of M_2CT_2 after Li_2S adsorption. The PDOS of M_2CT_2 monolayer after the adsorption of Li_2S are shown in Fig. 7. Compared with the PDOS of M_2CT_2 monolayer, the Fermi level of M_2CT_2-Li_2S has shifted upwards with the electronic state of S atoms appearing in the band gap for the Mo_2CF_2−, Cr_2CF_2−, Mn_2CO_2−, Mo_2CO_2−, and Cr_2CO_2-Li_2S systems. Therefore, the band gap of V_2CF_2 and Cr_2CF_2 became narrow, while Mo_2CF_2, Cr_2CO_2, and Mn_2CO_2 exhibit metallic characters after the adsorption of Li_2S. Overall, the conductivity of M_2CT_2 is enhanced with the adsorption of Li_2S, which is benefit for the electron transportation.

Electrocatalysis of M_2CT_2 on discharge/charging kinetics

The chemisorption intensity of Li_2S_n species critically modulates electrochemical reaction kinetics. Overly robust binding interactions may restrict surface mobility of redox-active intermediates, consequently impairing charge transfer efficiency. Such kinetic constraints during sulfur redox cycling constitute a fundamental performance limitation in Li-S battery systems.[54,55] The SRR pathways on M_2CT_2 surfaces are systematically mapped through density functional theory (DFT) calculations, with the thermodynamic Gibbs free energy change (ΔG) for each reaction intermediate from S_8 to Li_2S quantitatively presented in Fig. 8 and Table S3.† The calculation route of the SRR refers to the previous reports.[51,52] Obviously, the steps from S_8 to Li_2S_8 are all spontaneous exothermal on all the calculated M_2CT_2, which indicates that the S_8 can be readily converted into Li_2S_8. All reduction steps from Li_2S_8 to Li_2S are found to be endothermic, with the sole exception of the Li_2S_6 → Li_2S_4 step. The rate-limiting step is identified as Li_2S_4 → Li_2S_2 for V_2CO_2, Mo_2CF_2, and Mo_2CO_2, whereas for V_2CF_2, Cr_2CF_2, Cr_2CO_2, Mn_2CF_2, and Mn_2CO_2, the Li_2S_2 → Li_2S step served as the kinetic bottleneck. The endergonic Li_2S_2 → Li_2S transition stems from the inherent kinetic limitations of solid-state conversion processes, aligning with established theoretical

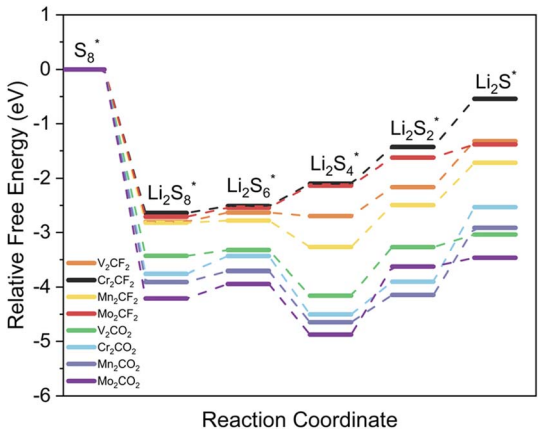

Fig. 8 The calculation of Gibbs free energy change (ΔG) of SRR on MXene monolayers.

frameworks in sulfur electrochemistry.[56,57] The Gibbs free energy change barrier ($\Delta G_{barrier}$) for the rate-limiting step follow the sequence: Mo_2CF_2 (0.51 eV) < Mn_2CF_2 (0.78 eV) < V_2CF_2 (0.84 eV) < Cr_2CF_2 (0.88 eV) < V_2CO_2 (0.89 eV) < Mn_2CO_2 (1.23 eV) < Mo_2CO_2 (1.25 eV) < Cr_2CO_2 (1.37 eV). It is easy to find that the M_2CF_2 have lower rate-limiting step reaction energy barrier than those of M_2CO_2, which proves that the F atom greatly enhances the catalytic activity of the SRR.

The elevated dissociation energy barrier of Li_2S, the terminal discharge product, significantly impedes electrochemical cycling reversibility.[58,59] This necessitates efficient delithiation kinetics ($Li_2S \rightarrow LiS + Li^+ + e^-$) to sustain charging efficiency. Fig. 9 quantitatively delineates the atomic-scale decomposition pathways of Li_2S on M_2CT_2 monolayers, revealing the critical decomposition energy barriers. The minimum decomposition barriers of Li_2S are 0.27, 0.32, 0.51, and 0.53 eV on Mo_2CO_2, V_2CO_2, Cr_2CO_2 and Mn_2CO_2, respectively, while they are 0.74, 0.80, 0.90, and 1.00 eV on Mn_2CF_2, Mo_2CF_2, V_2CF_2 and Cr_2CF_2, respectively. Similar to the decomposition barrier of Li_2S on $Ti_3C_2F_2$ (0.90 eV) and $Ti_3C_2O_2$ (0.41 eV),[60] all the M_2CT_2 greatly reduce the decomposition barriers, which indicate great catalytic effect for the decomposition reaction. Studies attribute this phenomenon to MXenes' metal-to-carbon (M/C) ratio, where elevated transition metal content (M) enhances Li_2S dissociation kinetics through optimized d-band electronic interactions.[27] The results indicate that the M_2CT_2 could promote the decomposition of Li_2S, which enhances the electrochemical kinetics performance of Li-S batteries.

The charging mechanism initiates with the delithiation of the terminal discharge product Li_2S, where ion migration dynamics critically govern decomposition and nucleation processes. Of particular significance is the interfacial Li^+ diffusion kinetics across the cathode substrate, prompting systematic analysis of Li^+ migration energy barriers. Therefore, the activation energy barriers for Li^+ diffusion across the cathode are quantified through NEB simulations. Three kinds of the

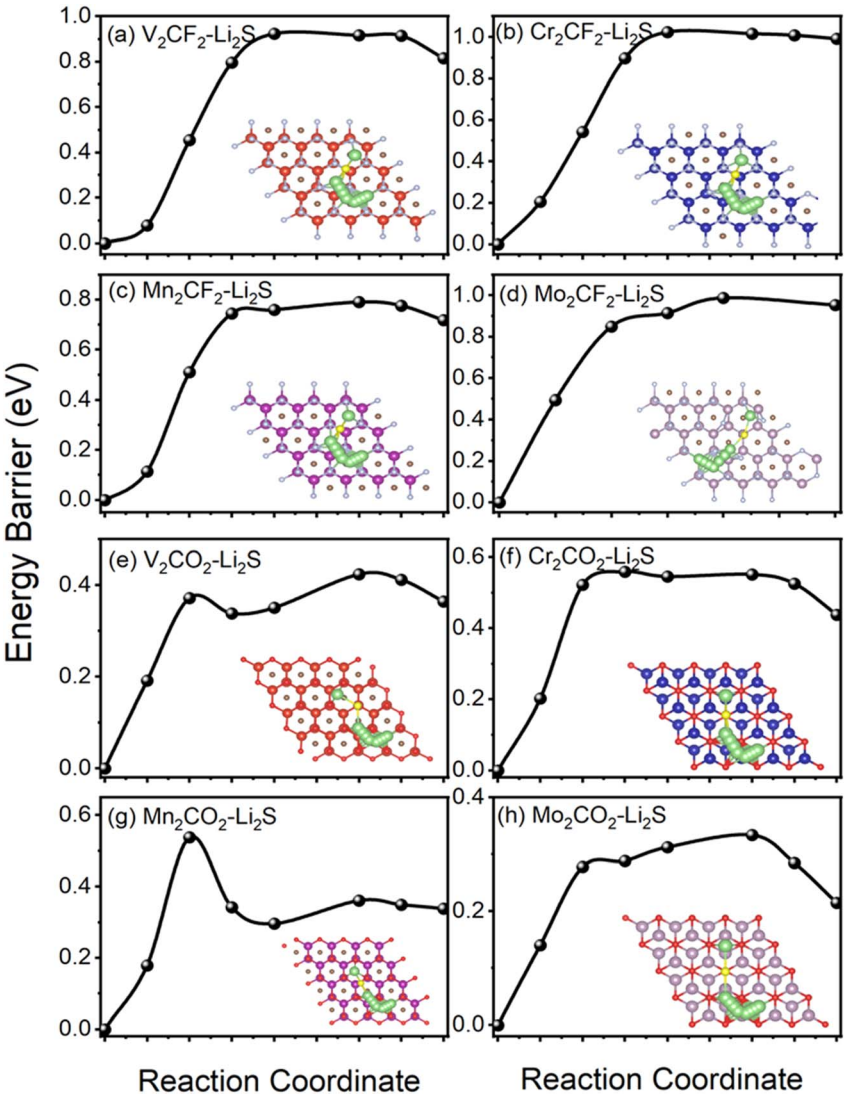

Fig. 9 Decomposition energies and decomposition paths of Li_2S on (a) V_2CF_2, (b) Cr_2CF_2, (c) Mn_2CF_2, (d) Mo_2CF_2, (e) V_2CO_2, (f) Cr_2CO_2, (g) Mn_2CO_2, and (h) Mo_2CO_2 monolayer.

migration paths of Li^+ are considered for Fcc and Hcp structure as presented in Fig. S5 (a) and (b),† respectively, and the diffusion barriers with different migration paths are shown in Fig. 10. It is found that the path 3 (the path 6) is the most difficult migration path for Fcc (Hcp) structure, while the diffusion barriers of the path 1 (the path 4) and the path 2 (the path 5) are comparable for all the calculated M_2CT_2. As shown in Fig. S5,† on V_2CT_2, Cr_2CF_2, Mn_2CT_2 and Mo_2CF_2, the Li^+ tend to move along the path 2 (C1 → M → C2), while on Cr_2CO_2 and Mo_2CO_2, the Li^+ prefers to be along the path 5 (H1 →C→ H2). The smallest diffusion barriers of Li^+ on the different M_2CT_2 follow the sequence: Mo_2CO_2 (0.11 eV) < Cr_2CO_2 (0.12 eV) < V_2CO_2 (0.13 eV) < Mn_2CF_2 (0.16 eV) < Mn_2CO_2 (0.25 eV) < V_2CF_2 (0.32 eV) < Cr_2CF_2 (0.33 eV) < Mo_2CF_2 (0.44 eV). These relatively low diffusion barriers of Li^+ promise the rapid diffusion of Li^+ on the M_2CT_2 surface and conversion of LiPSs during the charge process.

The decomposition of Li_2S, the diffusion of Li^+, and the catalytic activity of the SRR of the studied M_2CT_2 are compared with that of the available F/O-functionalized MXenes as listed in Table S4.† (ref. 27 and 61) It is found that the decomposition barriers of Li_2S for M_2CT_2 (0.27–1.00 eV) are apparently lower than those of V_2NF_2 (2.31 eV), V_2NO_2 (1.55 eV), and graphene (1.81 eV). Regarding the migration dynamics of Li^+, the diffusion barriers of Li^+ on the M_2CT_2 substrate (0.11 eV–0.44 eV) are close to those of V_2NF_2 (0.17 eV), V_2NO_2 (0.21 eV), and graphene (0.30 eV). Thus, M_2CT_2 show great kinetic performance during the discharge/charging process with relatively small decomposition barriers of Li_2S and diffusion barriers of Li^+. What's more, the $\Delta G_{barrier}$ of M_2CT_2 (0.51 eV–1.37 eV) are significantly lower than those of V_2NF_2 (2.14 eV) and V_2NO_2 (1.88 eV), while they are comparable or lower than that of graphene (1.07 eV). Considering the above factors, V_2CO_2 and Mo_2CO_2 have the best electrocatalytic performance among the studied M_2CT_2, in

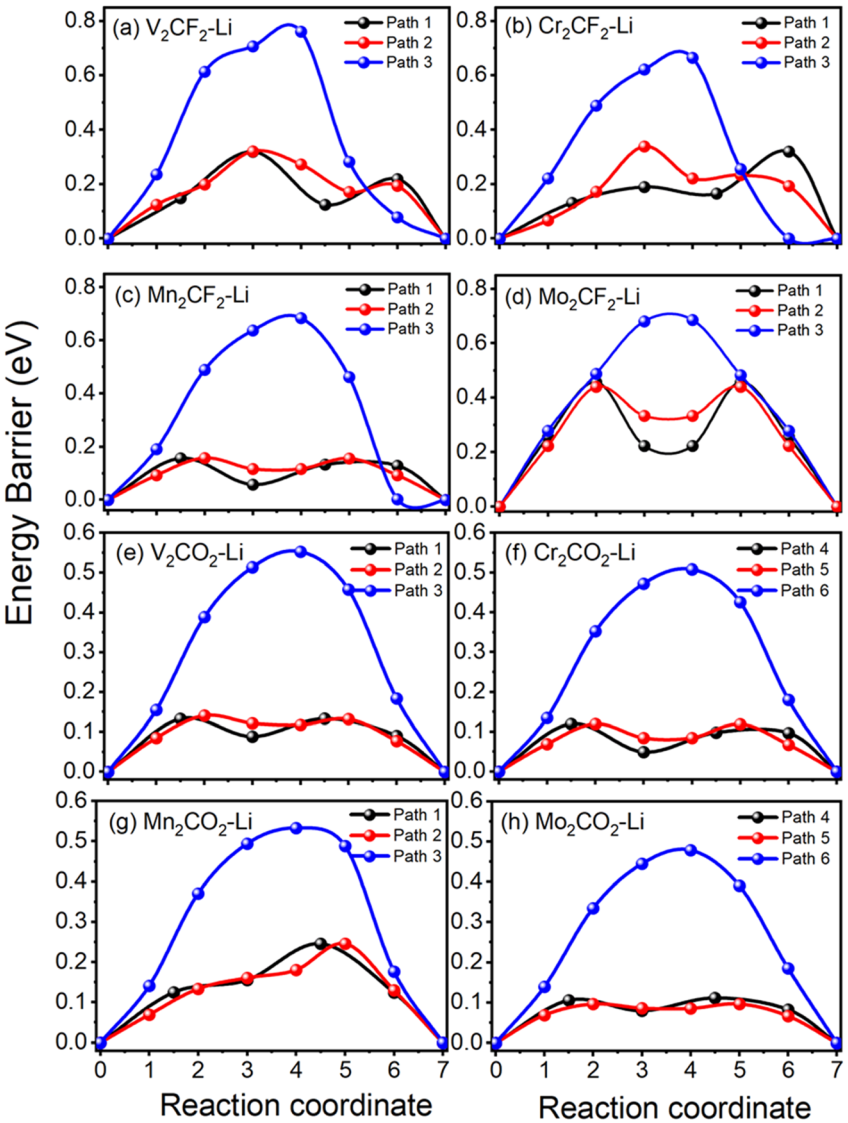

Fig. 10 Diffusion barriers with different migration paths of Li^+ on (a) V_2CF_2, (b) Cr_2CF_2, (c) Mn_2CF_2, (d) Mo_2CF_2, (e) V_2CO_2, (f) Cr_2CO_2, (g) Mn_2CO_2, and (h) Mo_2CO_2 monolayer.

which the decomposition barriers of Li_2S of V_2CO_2 and Mo_2CO_2 are only 0.32 eV and 0.27 eV, respectively, and the diffusion barriers of Li^+ of V_2CO_2 and Mo_2CO_2 are 0.13 eV and 0.11 eV, respectively. Moreover, the V_2CO_2 and Mo_2CO_2 are metallic, which is beneficial for a fast charge/discharge rate. Therefore, V_2CO_2 and Mo_2CO_2 are the best choices for Li-S battery cathode material in the studied M_2CT_2.

The structural stability of electrode materials critically determines their cycling lifespan within operational voltage windows. To further investigate the stability as cathode materials for Li-S batteries, we calculate the energy of Li_2S adsorption on V_2CO_2 and Mo_2CO_2 through AIMD simulations at room temperature (300 K). As illustrated in Fig. S6,† the total energy fluctuations progressively diminish during simulation, while the structural frameworks remain intact throughout the process. Therefore, it is demonstrated that both V_2CO_2 and Mo_2CO_2 maintain excellent thermodynamic stability with Li_2S adsorption, and further validated their promise as highly prospective host materials for Li-S batteries.

Conclusion

In summary, we systematically explore potential of M_2CT_2 (M = V, Cr, Mn, and Mo; T = F and O) as anchoring materials and catalysts for Li-S batteries using DFT spin-polarized calculations. A moderate E_{ads} for Li_2S_n on M_2CT_2 species are observed, which would restrain the shuttling of LiPSs and prevent capacity fading and enhance the cycling capability for Li-S batteries. The decomposition barriers of Li_2S (0.27 to 1.00 eV) and the Li^+ diffusion barriers of M_2CT_2 (0.11 to 0.44 eV) are relatively low, which would accelerate the formation and decomposition of solid Li_2S and hence redox reaction kinetics. It is also found that the M_2CO_2 exhibit lower decomposition barriers of Li_2S and diffusion barriers of Li^+ than M_2CF_2, especially for V_2CO_2 and Mo_2CO_2. Moreover, the structures of Li_2S adsorbed V_2CO_2 and Mo_2CO_2 exhibit good thermodynamic stability at room temperature. All studied M_2CT_2 exhibit relatively low $\Delta G_{barrier}$ during the reaction process (0.51 to 1.37 eV), which would promote the conversion of LiPSs. Generally, the studied oxygen-terminated MXenes exhibit superior electrochemical performance compared to their fluorine-terminated MXenes. V_2CO_2 and Mo_2CO_2 are identified as the most promising candidates for Li-S battery host materials in the explored M_2CT_2. Our study not only provides critical insights for advancing M_2CT_2 implementation in Li-S battery cathodes, but also expands further theoretical investigations into MXene-based materials.

Data availability

The data that supports the findings of this study are available from the corresponding author upon reasonable request.

Conflicts of interest

There are no conflicts to declare.

Acknowledgements

This work is supported by the National Natural Science Foundation of China (No. 11904409 and 51572296), Youth Innovation Technology Project of Higher School in Shandong Province (2022KJ139), Postdoctoral Research Foundation of China (No. 2018M642721), and Shandong Postdoctoral Funded Project (201901012).

References

1 B. Ding, J. Wang, Z. Fan, S. Chen, Q. Lin, X. Lu, H. Dou, A. Kumar Nanjundan, G. Yushin, X. Zhang and Y. Yamauchi, *Mater. Today*, 2020, **40**, 114–131.
2 W. Jin, X. Zhang, M. Liu, Y. Zhao and P. Zhang, *Energy Storage Mater.*, 2024, **67**, 103223.
3 R. Kumar, J. Liu, J.-Y. Hwang and Y.-K. Sun, *J. Mater. Chem. A*, 2018, **6**, 11582–11605.
4 A. D. Pathak, E. Cha and W. Choi, *Energy Storage Mater.*, 2024, **72**, 103711.
5 S. C. Kim, X. Gao, S. L. Liao, H. Su, Y. Chen, W. Zhang, L. C. Greenburg, J. A. Pan, X. Zheng, Y. Ye, M. S. Kim, P. Sayavong, A. Brest, J. Qin, Z. Bao and Y. Cui, *Nat. Commun.*, 2024, **15**, 1268.
6 Z. Lv, P. Wang, J. Wang, S. Tian and T. Yi, *J. Ind. Eng. Chem.*, 2023, **124**, 68–88.
7 J. Li, Y. Qu, C. Chen, X. Zhang and M. Shao, *Nanoscale*, 2021, **13**, 15–35.
8 J. T. Kim, A. Rao, H. Y. Nie, Y. Hu, W. Li, F. Zhao, S. Deng, X. Hao, J. Fu, J. Luo, H. Duan, C. Wang, C. V. Singh and X. Sun, *Nat. Commun.*, 2023, **14**, 6404.
9 Y. Chen, T. Wang, H. Tian, D. Su, Q. Zhang and G. Wang, *Adv. Mater.*, 2021, **33**, 2003666.
10 R. B. Nuwayhid, J. Yeom, H. O. Ford, Z. G. Neale, M. W. Swift, N. Bernstein, R. Carter and J. W. Long, *RSC Appl. Interfaces*, 2025, **2**, 472–483.
11 Z. Wu, M. Liu, W. He, T. Guo, W. Tong, E. Kan, X. Ouyang, F. Qiao, J. Wang, X. Sun, X. Wang, J. Zhu, A. Coskun and Y. Fu, *Nat. Commun.*, 2024, **15**, 9535.
12 J. Chai, J. Du, Q. Li, N. Han, W. Zhang and B. Tang, *Energy Fuel.*, 2021, **35**, 15455–15471.
13 S. Li, D. Leng, W. Li, L. Qie, Z. Dong, Z. Cheng and Z. Fan, *Energy Storage Mater.*, 2020, **27**, 279–296.
14 Y. Pan, Y. Zhu, Y. Li, H. Liu, Y. Cong, Q. Li and M. Wu, *Appl. Surf. Sci.*, 2023, **610**, 155507.
15 M. Naguib, M. Kurtoglu, V. Presser, J. Lu, J. Niu, M. Heon, L. Hultman, Y. Gogotsi and M. W. Barsoum, *Adv. Mater.*, 2011, **23**, 4248–4253.
16 W. Meng, X. Liu, H. Song, Y. Xie, X. Shi, M. Dargusch, Z.-G. Chen, Z. Tang and S. Lu, *Nano Today*, 2021, **40**, 101273.
17 X. Liang, A. Garsuch and L. F. Nazar, *Angew. Chem., Int. Ed.*, 2015, **54**, 3907–3911.
18 X. Zhao, M. Liu, Y. Chen, B. Hou, N. Zhang, B. Chen, N. Yang, K. Chen, J. Li and L. An, *J. Mater. Chem. A*, 2015, **3**, 7870–7876.
19 W. Cui, Z.-Y. Hu, R. R. Unocic, G. Van Tendeloo and X. Sang, *Chin. Chem. Lett.*, 2021, **32**, 339–344.

20 Q. Yang, S. J. Eder, A. Martini and P. G. Grützmacher, *npj Mater. Degrad.*, 2023, **7**, 6.
21 D. Rao, L. Zhang, Y. Wang, Z. Meng, X. Qian, J. Liu, X. Shen, G. Qiao and R. Lu, *J. Phys. Chem. C*, 2017, **121**, 11047–11054.
22 J. Hu, B. Xu, C. Ouyang, S. A. Yang and Y. Yao, *J. Phys. Chem. C*, 2014, **118**, 24274–24281.
23 X. Liu, X. Shao, F. Li and M. Zhao, *Appl. Surf. Sci.*, 2018, **455**, 522–526.
24 H. Lin, D.-D. Yang, N. Lou, S.-G. Zhu and H.-Z. Li, *Ceram. Int.*, 2019, **45**, 1588–1594.
25 C. Shi, X. Zhang, Z. Li, T. T. Beyene, T. Zheng, Y. Liu and K. Zhu, *Energy Fuels.*, 2024, **38**, 14866–14890.
26 Q. Zhang, X. Zhang, Y. Xiao, C. Li, H. H. Tan, J. Liu and Y. Wu, *ACS Omega*, 2020, **5**, 29272–29283.
27 D. Wang, F. Li, R. Lian, J. Xu, D. Kan, Y. Liu, G. Chen, Y. Gogotsi and Y. Wei, *ACS Nano*, 2019, **13**, 11078–11086.
28 C. Lamiel, I. Hussain, J. H. Warner and K. Zhang, *Mater. Today*, 2023, **63**, 313–338.
29 L. Zhang, J. Shi, K. Niu, P. Jia, Y. Gao and G. Gao, *ACS Appl. Nano Mater.*, 2023, **6**, 20812–20822.
30 G. F. l. Kresse, *Phys. Rev. B:Condens. Matter Mater. Phys.*, 1996, **54**, 11169–11186.
31 J. P. B. Perdew and K. Burke, *Phys. Rev. Lett.*, 1996, **77**, 3865–3868.
32 G. F. l. Kresse, *Comput. Mater. Sci.*, 1996, **6**, 15–50.
33 V. I. Anisimov and a. O. K. A. Jan Zaanen, *Phys. Rev. B:Condens. Matter Mater. Phys.*, 1991, **44**, 943–954.
34 S. Bae, Y. G. Kang, M. Khazaei, K. Ohno, Y. H. Kim, M. J. Han, K. J. Chang and H. Raebiger, *Mater. Today Adv.*, 2021, **9**, 100118.
35 Q. Sun, Z. Fu and Z. Yang, *J. Magn. Magn. Mater.*, 2020, **514**, 167141.
36 X. Zhang, W. Meng, T. He, L. Jin, X. Dai and G. Liu, *Appl. Surf. Sci.*, 2020, **503**, 144091.
37 S. Grimme, J. Antony, S. Ehrlich and H. Krieg, *J. Chem. Phys.*, 2010, **132**, 154104.
38 G. U. Henkelman, B. P. Uberuaga and H. Jónsson, *J. Chem. Phys.*, 1991, **113**, 9901–9904.
39 M. Khazaei, M. Arai, T. Sasaki, C. Y. Chung, N. S. Venkataramanan, M. Estili, Y. Sakka and Y. Kawazoe, *Adv. Funct. Mater.*, 2012, **23**, 2185–2192.
40 P. Gao, M. Song, X. Wang, Q. Liu, S. He, Y. Su and P. Qian, *Nanomaterials*, 2022, **12**, 556.
41 J. He, P. Lyu and P. Nachtigall, *J. Mater. Chem. C*, 2016, **4**, 11143–11149.
42 Q. Sun, Z. Fu, Y. Li and Z. Yang, *J. Alloys Compd.*, 2021, **850**, 156769.
43 Z. Tan, Z. Fang, B. Li and Y. Yang, *ACS Omega*, 2020, **5**, 25848–25853.
44 L. Zhang, Y. Liu, M. Wu and G. Gao, *Adv. Funct. Mater.*, 2024, 2417857.
45 L. Zhang, Y. Liu, Z. Xu and G. Gao, *2D Mater.*, 2023, **10**, 045005.
46 C. Zhang, W. Chu, X. Hong, Q. He, R. Lu, X. Liao and Y. Zhao, *Chem. Eng. J.*, 2022, **439**, 135679.
47 G. Xu, X. Song, M. Jiang, R. Wang, S. Lian and X. Yang, *Appl. Catal., B*, 2025, **362**, 124707.
48 Z. Chen, S. Huang, X. Yuan, X. Gan and N. Zhou, *Appl. Surf. Sci.*, 2021, **544**, 148861.
49 Z. Chen, S. Huang, B. Huang, M. Wan and N. Zhou, *Appl. Surf. Sci.*, 2020, **509**, 145319.
50 Z. Chen, Z. Chang, Z. Liu and N. Zhou, *Appl. Surf. Sci.*, 2022, **602**, 154375.
51 X. Zhu, M. Ge, T. Sun, X. Yuan and Y. Li, *J. Phys. Chem. Lett.*, 2023, **14**, 2215–2221.
52 C. Wei, T. Fang, X. Tang, P. Wang and X. Liu, *J. Phys. Chem. C*, 2022, **126**, 17066–17075.
53 M. Cheviri and S. Lakshmipathi, *Comput. Theor. Chem.*, 2021, **1202**, 113323.
54 Z. Du, X. Chen, W. Hu, C. Chuang, S. Xie, A. Hu, W. Yan, X. Kong, X. Wu, H. Ji and L. J. Wan, *J. Am. Chem. Soc.*, 2019, **141**, 3977–3985.
55 G. Zhou, S. Zhao, T. Wang, S. Z. Yang, B. Johannessen, H. Chen, C. Liu, Y. Ye, Y. Wu, Y. Peng, C. Liu, S. P. Jiang, Q. Zhang and Y. Cui, *Nano Lett.*, 2020, **20**, 1252–1261.
56 Z. Yi, F. Su, L. Dai, Z. Wang, L. Xie, Z. Zuo, X. Chen, Y. Liu and C.-m. Chen, *Energy Storage Mater.*, 2022, **47**, 327–335.
57 Z. Jin, T. Lin, H. Jia, B. Liu, Q. Zhang, L. Li, L. Zhang, Z. M. Su and C. Wang, *ACS Nano*, 2021, **15**, 7318–7327.
58 Y. Fu, H. Wang, D. Li, J. Shen, Y. Liu, M. Wei and Q. Hu, *J. Alloys Compd.*, 2023, **965**, 171306.
59 X. T. Fang, L. Zhou, C. Chen, D. L. Danilov, F. Qiao, H. Li and P. H. L. Notten, *Molecules*, 2023, **28**, 7304.
60 H. Hong, N. A. R. Che Mohamad, K. Chae, F. Marques Mota and D. H. Kim, *J. Mater. Chem. A*, 2021, **9**, 10012–10038.
61 K. Fan, Y. Ying, X. Luo and H. Huang, *J. Mater. Chem. A*, 2021, **9**, 25391–25398.